Microstructure investigation of magnetron sputtered WC/C coatings deposited on steel substrates

Carvalho, N.J.M.; de Hosson, J.T.M.

Published in:
Thin Solid Films

DOI:
10.1016/S0040-6090(01)00842-2

Publication date:
2001

ELSEVIER

Thin Solid Films 388 (2001) 150–159

thin solid films

www.elsevier.com/locate/tsf

Microstructure investigation of magnetron sputtered WC/C coatings deposited on steel substrates

N.J.M. Carvalho, J.Th.M. DeHosson*

Department of Applied Physics and Netherlands Institute of Metals Research, University of Groningen, Nijenborgh 4, 9747 AG Groningen, The Netherlands

Received 7 July 2000; received in revised form 16 December 2000; accepted 6 February 2001

Abstract

Electron microscopy, including scanning (SEM), transmission (TEM) and high-resolution (HRTEM) were employed to characterise slightly different tungsten carbide/carbon coatings deposited onto steel substrates. Complementary techniques, such as X-ray diffraction (XRD), Auger electron spectroscopy (AES) and energy filtered TEM (GIF) were also used. The coatings were deposited by magnetron sputtering of pure WC and Cr targets in a plasma decomposition of C_2H_2 in mixed Ar–C_2H_2 discharges. The coatings are made up of a chromium interlayer, a coarse WC/C intermultilayer, a WC layer, and the WC/C multilayer. The chromium interlayer has a body centred cubic phase and a dense columnar structure, while the remaining coating is truly amorphous, with the exception of polycrystalline particles and clusters that are present within some layers. Crystalline particles and clusters were identified as having the cubic β-WC_{1-x} phase. Defects in the coatings were also found, due to substrate surface irregularities and to the growth structure of the chromium columns.

Keywords: Multilayers; Sputtering; Steel; Transmission electron microscopy; Auger electron spectroscopy

1. Introduction

New trends in mechanical engineering are leading to more stringent demands on machine components. The reduction of friction to increase the efficiency of motors, the improvement of the reliability of gears and roller bearings, and the reduction of hazardous lubricants are of major concern in the design of machinery. These trends might cause higher tribological stresses on components because higher loads, closer tolerances, or the reduction of lubricant can lead to adhesive wear of surfaces. One way to cope with these trends is to improve the surface properties by applying a thin low-friction high-wear-resistance solid film onto the machine components. Among others, molybdenum sulfide [1,2], and diamond-like carbon [3–5] have shown the most promising results. The main properties of these coatings include low static and dynamic friction coefficients against most metals and ceramics, chemical inertness, resistance to corrosive attack in acid or saline media, and high wear resistance. DLC coatings are formed by small clusters of microcrystalline structure with sp^3 and sp^2 bonding, embedded in an amorphous sp^3-bonded carbon matrix [6]. They have been studied since the 1970s and several different types of DLC have emerged. The most noteworthy are: pure DLC, hydrogen-free (i-C), hydrogenated (a-C:H), and metal-doped or carbide-doped (Me-C:H) amorphous carbon coatings. The dissimilarity between hydrogen-free and hydrogenated coatings, resides in the proportion of sp^3 bonds, being 85–95% for hydrogen-free and 30–60%

* Corresponding author. Tel.: +31-50-363-4898; fax: +31-50-363-4881.

E-mail address: hossonj@phys.rug.nl (J.Th.M. DeHosson).

0040-6090/01/$ - see front matter
PII: S0040-6090(01)00842-2

for hydrogenated. It is believed that the presence of hydrogen atoms play a crucial role in the bonding configuration by promoting and stabilising sp^3 tetrahedral bonds of the carbon atoms, which is suggested by some authors to be the origin of the high hardness of DLC coatings [7,8]. Metal-doped and carbide-doped DLC have received considerable attention in recent years, owing to their low friction coefficient and high wear resistance in combination with substrate temperatures of some 200–400°C during deposition. Furthermore, the fact that adhesion between the coating and the substrate has been improved by depositing an interlayer of chromium or molybdenum [9], has helped to promote the deposition of such coatings onto machine components subjected to a high shear stress component.

Tungsten carbide/carbon (WC/C) is an example of a multilayer structure composed of carbide-doped hydrogen and hydrogenated DLC lamellae. This coating has been reported to have successful engineering applications where low friction and high wear resistance are important requirements [10,11]. However, if the advantages are to be fully employed in improving the surface properties of engineering components, it is necessary to understand more thoroughly the detailed mechanisms by which surface properties are changed and enhanced.

The work presented in this paper is part of a broader study aiming to get a better understanding of the interplay between the chemical composition, the microstructure, and the mechanical properties of the coating/substrate system. Therefore, here we address the chemical composition and the microstructure of dissimilar WC/C coatings and their interface to steel substrates. Moreover, the predominant features and dissimilarities between the different coatings, which can be crucial for their performance, will be highlighted throughout the text. A thorough assessment of the elastic, plastic and fracture properties of each coated system based on nanoindentation experiments and on the outcome of this paper is under preparation.

Transmission electron microscopy (TEM) — in conventional and high-resolution mode — was used as primary technique. By combining direct imaging and electron diffraction, it was possible to obtain detailed information about phase composition, grain size and shape, and degree of preferred orientation. Nevertheless, complementary techniques such as analytical transmission electron microscopy, scanning electron microscopy (SEM), X-ray diffraction (XRD), and Auger electron spectroscopy (AES) were also used, providing additional invaluable information concerning the morphology, phase composition, and microchemistry of the coated systems.

2. Experimental details

2.1. Substrate materials

The coatings examined in this work were deposited onto stainless (AISI 304) and tool (AISI D2) steels. The substrates had both circular (60 mm external diameter, 13 mm thick) and rectangular ($90 \times 10 \times 3$ mm) geometries. The martensitic substrates were heat treated and tempered at 520°C to obtain 60 HRc. The substrate surfaces were finished by polishing to an average roughness, R_a, of 0.03, 0.05 and 0.07 μm, as listed in Table 1.

2.2. Deposition method

Three dissimilar WC/C coatings, denoted S1, S2 and T1, were deposited in a BAI 830 coating unit by Balzers Ltd, Liechtenstein. The combinations of coating/substrate evaluated in this study are presented in Table 1.

The deposition process consists of using DC magnetron sputtering of a pure WC target, with argon as a sputtering gas. The carbon phase was grown from plasma containing both hydrocarbon gas (acetylene, C_2H_2) and argon. The process utilised six planar magnetrons arranged in a circle, with the substrate passing consecutively performing a planetary rotation (i.e. also rotating on its own axis). The residual pressure in the deposition chamber was of the order of 10^{-3} Pa for all coatings. The samples were heated by radiation with a high current electron beam to a temperature in the range of 300–350°C. One chromium and five WC targets were employed. For all coatings an interlayer of chromium was initially formed by DC magnetron sputtering of a chromium target using an argon pressure of 0.62 Pa. Subsequently, the WC/C layer commenced deposition, i.e. DC magnetron sputtering of the WC targets started — at the same argon pressure — and acetylene with a partial pressure of 0.03 Pa was intro-

Table 1
Coated systems investigated in this work

Sample ID	Substrate material	Substrate hardness HV (GPa)	Substrate roughness Ra (μm)	Coating thickness (μm)	Coating roughness Ra (μm)
S1	Stainless steel (AISI 304)	1.6	0.05	3	0.05
S2	Stainless steel (AISI 304)	1.6	0.03	2.8	0.05
T1	Tool steel (AISI D2)	6.8	0.07	2.7	0.06

duced into the chamber. The deposition system and process have been described earlier by Farges et al. [12].

2.3. Characterisation techniques

The coatings were structurally characterised by X-ray diffraction (XRD), Auger electron spectroscopy (AES), energy dispersive X-ray spectroscopy (EDS), scanning electron microscopy (SEM) and transmission electron microscopy (TEM). The XRD measurements were carried out using a Philips PW710 based diffractometer with Cu-Kα radiation in $\theta/2\theta$ mode and generator settings of 40 kV and 30 mA.

Compositional AES line profiles on cross-sectional samples were performed with a JEOL JAMP 7800F, a combined UHV-Scanning-Auger/electron microscope (SEM/SAM) system equipped with a hemispherical analyser (HAS). Typically, the electron beam current was 2.2 nA at 10 kV accelerating voltage, generated by a field emission gun (FEG). These conditions yield a beam spot size of $\sim$15 nm, allowing a lateral resolution down to nanometer length scales. The samples were prepared in a similar way to the cross-sectional TEM (XTEM) specimens. This procedure enables the area of interest to be evenly smooth and clean from contaminants. Prior to Auger data collection the samples were Ar^+-ion sputtered to remove any possible remaining oxide layer. In order to make the intensity in the direct AES spectra approximately quantitative, the Auger signal was obtained using the function $(N_1 - N_2)/(N_1 + N_2)$, where N_1 is the signal on an Auger electron peak and N_2 is that on the background at slightly higher energy. This function has an excellent signal-to-noise behaviour and largely removes topographical effects that might be present in line profiles [13].

The coating morphology was examined using a SEM (Philips FEG-XL 30) on plan-view and cross-sectional samples, either polished or fractured. Specimen preparation for XTEM consisted of gluing two samples film-to-film in a 700-μm-wide slot of a Ti disc. Subsequently, the sample was mechanically ground and polished on both sides to a thickness of $\sim$50 μm. This was followed by ion beam milling using two guns in mirror-image positions on both sides of the sample. The angle of incidence was 6° (ion energy 4 kV and ion current 40 μA) and the specimen was rotated. Final thinning to electron transparency was accomplished by rocking the specimen $\pm$30° perpendicular to the coating/substrate interface with an incoming ion beam at 4°. This process continued until perforation took place and the hole reached the area of interest. Finally, the surface contaminants (due to redeposited material) were reduced by using an ion energy of 2 kV and ion current of 4 μA while continuing rocking the specimen. After this final cleaning process, which took approximately 20 min, large electron transparent areas with low surface contamination were achieved.

Analytical transmission electron microscopy was carried out using a JEOL 2010 FEG, operating at 200 kV, equipped with an EDAX energy dispersive analyser and a post-column Gatan Imaging Filter (GIF). EDS analysis were performed by line profile in XTEM specimens using a normal probe with FWHM of 0.5 nm. The distance between points was varied depending on the layer thickness, ranging from 3.8 nm in the WC/C multilayer to 10.7 nm in the chromium interlayer. Electron-energy-filtered images were recorded using the Cr–L_3 edge for Cr-mapping, Fe–L_3 edge for Fe-mapping and C–K edge for C-mapping. One post-edge and two pre-edge images were acquired using a slit width of 30 eV for Cr, 40 eV for Fe and 20 eV for C. A background image was estimated from the two pre-edge images and subtracted from the post-edge image. This procedure gave maps of edge intensity vs. position in the coating, i.e. an independent recording of the concentration profile.

High resolution TEM (HRTEM) observations were carried out using a JEOL 4000 EX/II, operating at 400 kV with a spherical aberration constant $C_S = 0.97$ mm and a wavelength of $\lambda = 1.64$ pm. All micrographs were acquired close to the minimum contrast defocus. The difference observed between this defocus value and the Scherzer value resided only on the granularity (noise) of the amorphous material. Since it was much coarser at the Scherzer defocus, the former value was adopted throughout.

3. Results and discussion

3.1. Phases and structure

X-Ray diffraction (XRD) is widely used for structural analysis of coatings. However, the observed diffraction peaks are often quite broad due to small grain sizes and high defect concentrations in the coating. Hence, the precision of lattice constant determinations is generally not better than 0.01 Å [14]. However, as 0.01 Å accuracy is often sufficient for general phase identification, this technique was used to identify the phases present in the coatings. The diffraction peaks detected in XRD patterns for the three sets of coating/substrate evaluated, are displayed in Fig. 1. In the case of coating systems S1 and T1 the chromium (110) lattice plane provided the most intense peak, whereas in system S2 the (200) plane was the most intense. Therefore, the chromium interlayer of systems S1 and T1 has a (110) preferred orientation parallel to the surface, whereas system S2 has a (200) preferred orientation. All systems displayed a broad peak characteristic of an amorphous phase suggesting that the WC and

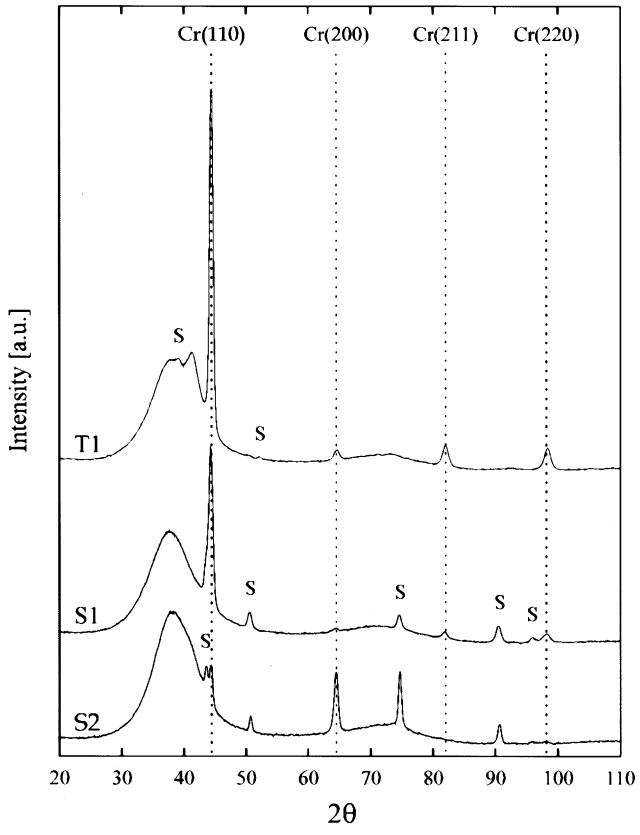

Fig. 1. X-Ray diffraction patterns of coated systems T1, S1 and S2. The reference positions of body centred cubic chromium phase and peaks from the steel substrates (labelled S) are indicated. The diffraction pattern of stainless steel consists mainly of γ-Fe and Fe–Cr–Ni phases, while for tool steel consists of α-Fe and chromium carbide, Cr_7C_3, phases.

carbon layers are both amorphous. The only exception is in system T1 where a single diffraction peak indicates the presence of a WC crystalline phase.

The morphology of the WC/C is disclosed by plan-view and cross-sectional SEM micrographs in Fig. 2. The coatings have a nodular surface morphology with growth defects — droplets — typical of PVD [12]. The surface grooves in the coating are due to irregularities on the underlying substrate, as can be attested by the cross-sectional micrographs. The substrate irregularities, grooves and ridges, were still present after the pre-treatment because the process was unidirectional. The polishing resulted in a smoother surface. However, it did not remove completely the deeper grooves or higher ridges. The coating thickness and surface roughness of the different sets of samples are presented in Table 1. The cross-sectional SEM micrographs were obtained with a backscattered electron (BSE) detector. Since the number of BSE increases with increasing atomic number, Fig. 2b,d,f revealed important insights regarding the coatings composition. Apparently, the concentration and distribution of tungsten, the element with higher atomic number, is different in the various coatings. Systems S1 and T1 are alike with respect to the thickness of the band with a higher tungsten concentration, whereas in system S2 the thickness is roughly twice. As can be promptly perceived, this difference in band thickness may have a direct influence on the elastic properties of the coatings. It is most probable that system S2 is the one with a lower elastic recovery response when subject to surface deformation.

The tungsten enrichment of the brighter band observed in BSE micrographs was cross-checked by an AES line profile. An AES line profile from the coating system T1 is shown in Fig. 3. It can be seen that both C and Cr Auger intensities are enhanced at the Cr layer. After that the W intensity increases, reaching a maximum in the brighter band, while the C is the inverse. The Cr drops to zero, indicating that the Cr deposition ceased. EDS analysis performed on XTEM specimens, also confirm the W and C concentration gradient at the WC layer. However, beyond this region their intensities are uniform through the remaining multilayer until roughly 0.5 μm from the top. From here on, the friction properties of the coating are enhanced by an increase of C and decrease of W. The sharp C signal at the edge of the sample is related to a change in surface orientation of the sample (edge of the cross-section) rather than a sudden increase in concentration.

The coating–substrate interface is shown by a HRTEM micrograph in Fig. 4. There is an amorphous interfacial region (approx. 5 nm thick) between the crystalline steel substrate and the columnar chromium. The interphase shows a relatively smooth top surface, whereas the interface to the underlying steel presents a slight roughness due to diffusion of chromium into steel. From a through-focal series of micrographs it was learned that the interphase showed no contrast reversal, i.e. the contrast did not change from bright to dark as the focus condition was changed from under- to over-focus. This indicates, that the interfacial region is made up of a high-atomic-density phase [15]. It is believed that this high-density interfacial contact allows a robust adhesion of the chromium layer to the substrate. Furthermore, the interphase initially has a higher contrast, suggesting that it is composed of a higher mass-thickness. All these considerations allow us to assume that first chromium diffused into the steel, to an extent of $\sim$2.5 nm, and then a pure amorphous chromium region was formed. Within this amorphous layer the columnar structure must have been nucleated.

The microstructures of the coating systems are presented by overview cross-sectional TEM micrographs in Fig. 5. Their structure is formed by a chromium interlayer, an intermultilayer, a WC layer, and finally a WC/C multilayer. The chromium interlayer has a dense columnar structure, typical of coatings grown under low energetic ion bombardment and limited adatom mobil-

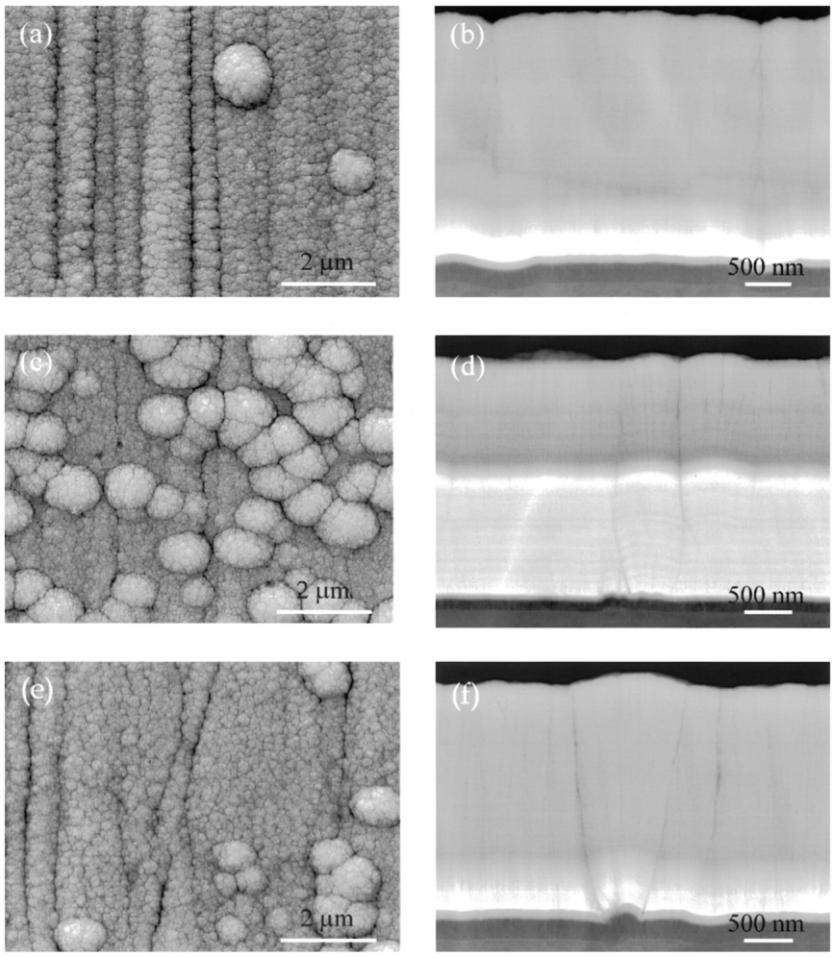

Fig. 2. Scanning electron micrographs displaying the morphology of WC/C coatings: (a and b) plan-view and cross-section micrographs from coating system S1, respectively; (c and d) micrographs from coating system S2; (e and f) micrographs from coating system T1. The plan-view micrographs illustrate the coating nodular surface morphology typical of PVD process and grooves created by the underlying substrate irregularities. The cross-sectional micrographs obtained with backscattered electron detector show differences dissimilarity in tungsten concentration within the multilayer.

ity conditions [16]. Their average thickness is ~205 nm, except in system S2 whose thickness is ~120 nm. The average column diameter is 22, 18 and 24 nm for system S1, S2 and T1, respectively. This indicates that the columns broaden with increasing layer thickness. Therefore, the column diameter can be explained considering the three stages of development of textures in PVD coatings: nucleation, competitive growth, and steady growth. Once the (110) orientation achieved dominance in the competitive growth at the expenses of the (200) orientation (cf. Fig. 1), — thought to occur after the first 100 nm — the interlayer grew steadily with this preferred orientation. The intermultilayer is fashioned by WC and carbon amorphous layers, corresponding to darker and brighter bands, respectively. For coating system S1 and T1 the intermultilayer is ~93 nm thick with a periodic wavelength, Λ, of ~15.5 nm. On the other hand, the intermultilayer of system S2 is thinner, ~50 nm. It has a different structure, comprising of three thicker carbon layers with thinner WC and carbon lamellae in between. The chromium columnar structure seems to have grown into all the intermultilayers distorting them by imposing a wavy structure with a period linked to the column diameter. As a result, nano-polycrystalline particles of chromium carbides were formed in the carbon layers. Flanked by the intermultilayer and the WC/C multilayer there is an amorphous WC layer with a thickness of ~200 nm in system S1 and T1. In the former, the layer is truly amorphous while within the latter polycrystalline columnar particles were grown. In addition, this layer is darker than the remaining coating, indicating that it has a higher mass-thickness. Altogether, these interfacial bond layers between the WC/C multilayer and the substrate are employed to provide a good adherence in applications where a high shear stress component is present [17]. The WC/C multilayer has an interlaminar structure with the darker lamellae being WC rich and the brighter lamellae carbon rich. Once again, the thickness of the interlaminants in systems S1

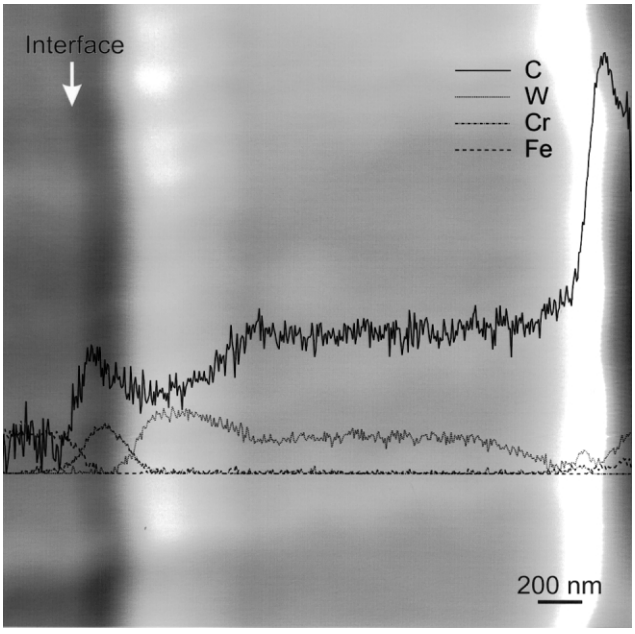

Fig. 3. Line profile of C_{KLL}, W_{MNN}, Cr_{LMM}, and Fe_{KLL} Auger intensity plotted as a function of coating thickness. The data, presented as measured, are superimposed on a SEM micrograph of coating system T1. The zero intensity line corresponds to the position where the data were taken. The arrow indicates the coating–substrate interface.

and T1 are roughly the same, ~6 nm for WC lamellae and ~2 nm for carbon. In the case of system S2 the multilayer was grown directly from the intermultilayer with Λ ~15.5 nm and a WC lamellae thickness of ~13 nm. From HRTEM, it was found that the multilayers have a different interlaminar structure. In the former two systems, the multilayer consists of an amorphous phase, whereas the latter is constituted of an amorphous matrix with clusters of crystalline particles

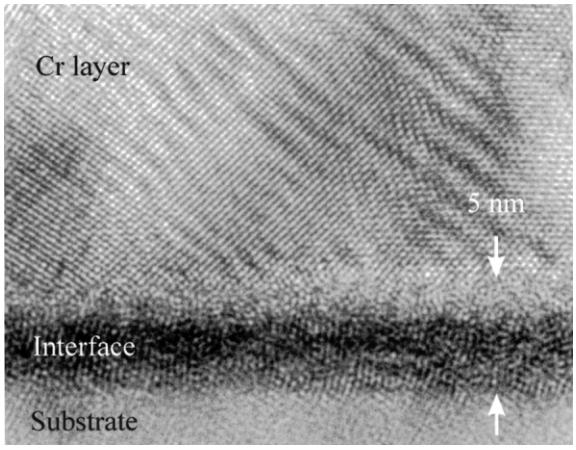

Fig. 4. Cross-sectional high-resolution transmission electron microscopy micrograph of the coating–substrate interface region of coating system T1. The interphase is similar to one of the other systems. The arrows indicate the position of the interphase.

embedded in the WC lamellae. The carbon lamellae have approximately the same thickness for the three coatings. However, the C–WC interface of the former systems is rather diffuse, whereas for system S2 the interface is sharper. These differences in lamellae thickness and sharpness of the interface have proved to be important in the performance of the coated systems by facilitating crack propagation or not.

3.2. Particles embedded in the coating's amorphous structure

The structure of the intermultilayer consists of WC and carbon layers, both being amorphous. However, in the latter, nano-polycrystalline particles were found. An example of such particles present in the carbon

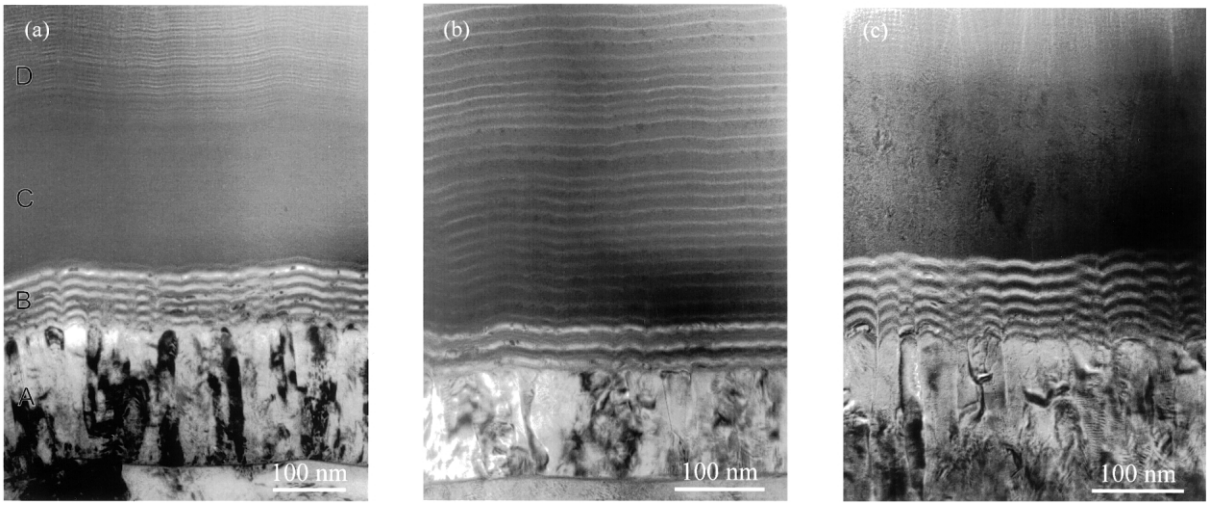

Fig. 5. Cross-sectional transmission electron microscopy micrograph showing the microstructure of the three coatings investigated in this study: (a) coating system S1; (b) coating system S2; (c) coating system T1. Their structure is constituted of a chromium interlayer (A), an intermultilayer (B), a WC layer (C) for systems S1 and T1, and the WC/C multilayer (D).

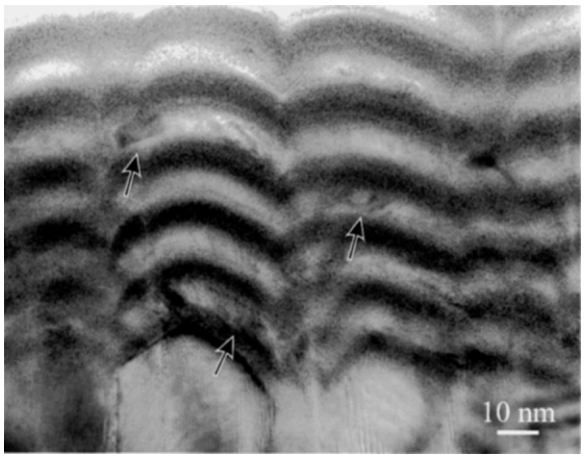

Fig. 6. Cross-sectional transmission electron microscopy micrograph of the intermultilayer from coating system T1. The darker bands correspond to WC, whereas the brighter correspond to carbon. In the latter, nano-polycrystalline chromium carbides are present due to growth of chromium into the layers (some are arrowed). Moreover, the morphology of the intermultilayer is related to the diameter and top morphology of the chromium columns. Planar defects were created at the interface of the columns whenever the columns presented a faceted top morphology.

layers is shown in Fig. 6. As can be observed, the structure of the layers is dependent on the interface roughness originating from the individual chromium columnar structure. It is interesting to note, that the shape of polycrystalline particles follow the morphology of the carbon layers and are only present in these ones. The formation of these particles can be attributed to some residual chromium atoms that might still be present in the coating chamber after the interlayer growth, and due to their high affinity for carbon, chromium carbide nano sized particles have been formed. This assumption is supported by electron energy filtered images of the intermultilayer, where chromium was mapped in the carbon layers. Other types of crystalline particles, which are embedded in the amorphous WC layer of system T1 are revealed in Fig. 7. These particles prevailed throughout the layer and have a structure similar to the one formed by ballistic aggregation on a point seed [18]. However, the void streaks often observed in the columnar structure, were replaced by stacking faults. The growth direction of the particles was parallel to the ⟨200⟩ direction and normal to the coating–substrate interface. From selected area electron diffraction pattern analysis it was possible to identify the structure of these particles as face centred cubic β-WC_{1-x}. This identification is also in agreement with the XRD pattern, where the diffraction peak unidentified in Fig. 1 corresponds to the (200) plane of the β-WC_{1-x}. As can be seen in the HRTEM inset, the crystal has a high density of stacking faults in the {111} planes. This fact, is related to the cubic β-WC_{1-x} phase being stable only for a carbon concentration of ~ 40 at.%, while for higher carbon content the hexagonal structure is more favourable [19]. Nevertheless, microchemical analysis performed by EDS showed that the particles present in the amorphous layer had an atomic concentration of carbon corresponding to the hexagonal structure. Therefore, the intrinsic stacking faults in the close packed {111} planes are formed to

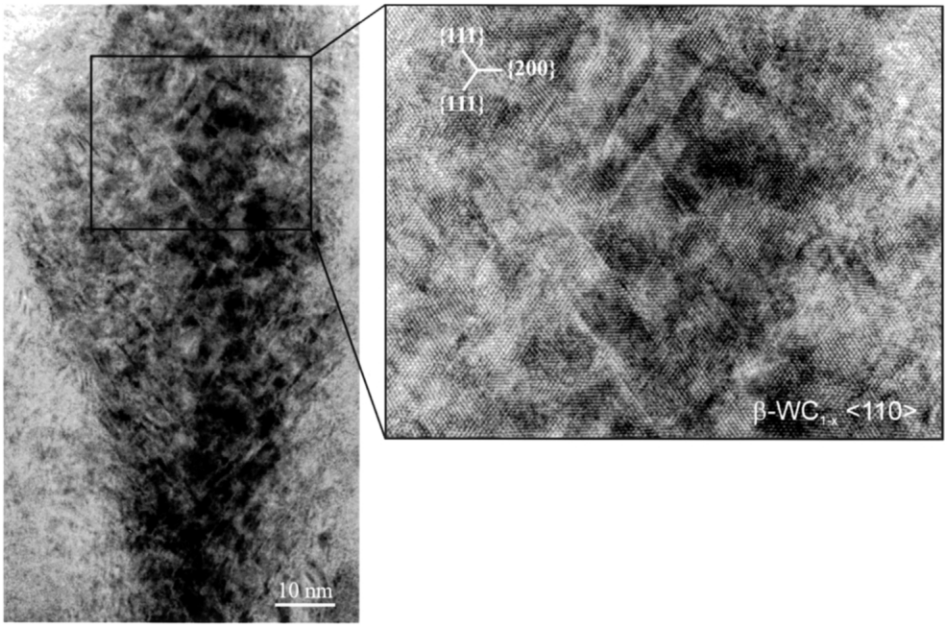

Fig. 7. Overview cross-sectional transmission electron microscopy micrograph of a crystalline columnar particle embedded in the amorphous WC layer from coating system T1. The particle is viewed along the ⟨110⟩ zone axis and was identified as having a cubic β-WC_{1-x} phase. The high-resolution inset shows the intrinsic stacking faults in the {111} planes.

allow a local transformation of the cubic structure into hexagonal.

The WC/C multilayer from coating system S2 is constituted by an amorphous interlaminar structure with clusters of crystalline particles entrenched in the WC lamellae. Fig. 8a shows a HRTEM micrograph from an area of the multilayer containing nano-crystalline particles. The particles are equally distributed throughout the multilayer, having a relatively constant diameter of 4–10 nm. Their position in the lamella is always shifted slightly towards the upper part. This observation, allows to assume that the nucleation did not occur at the first WC atomic layers because the interface with the previous carbon lamella was not sharp, owing to interdiffusion of the latter. Therefore, as the nucleation started roughly in the middle of the lamella and was ceased by the growth of the next carbon lamella, the particles have, obviously, a smaller size than the lamellae thickness. Given the relatively small particle size it was impossible to determine the crystal structure and hence their phase either by XRD analysis or selected area electron diffraction. Thus, to calculate the structure of the clusters, Fourier transformation from the HRTEM micrographs was applied to obtain the diffraction pattern. Subsequently, the diffraction pattern was rotated to get rings from the symmetrically distributed diffraction points, and the interplanar spacings corresponding to the lattice points were measured. The same method was applied to the crystals present in the WC layer of system T1, and both were compared. The result allowed us to conclude that the clusters present in the WC lamellae of system S2 have the same phase-cubic β-WC_{1-x} — as the crystals present in the WC layer of system T1. In the other coating systems, the WC lamellae does not have particles present, which is believed to be related to their reduced thickness of ~ 6 nm not enabling particle nucleation and growth. Fig. 8b shows a HRTEM micrograph of the multilayer from coating system S1, depicting the amorphous nature of the lamellae without clusters of particles.

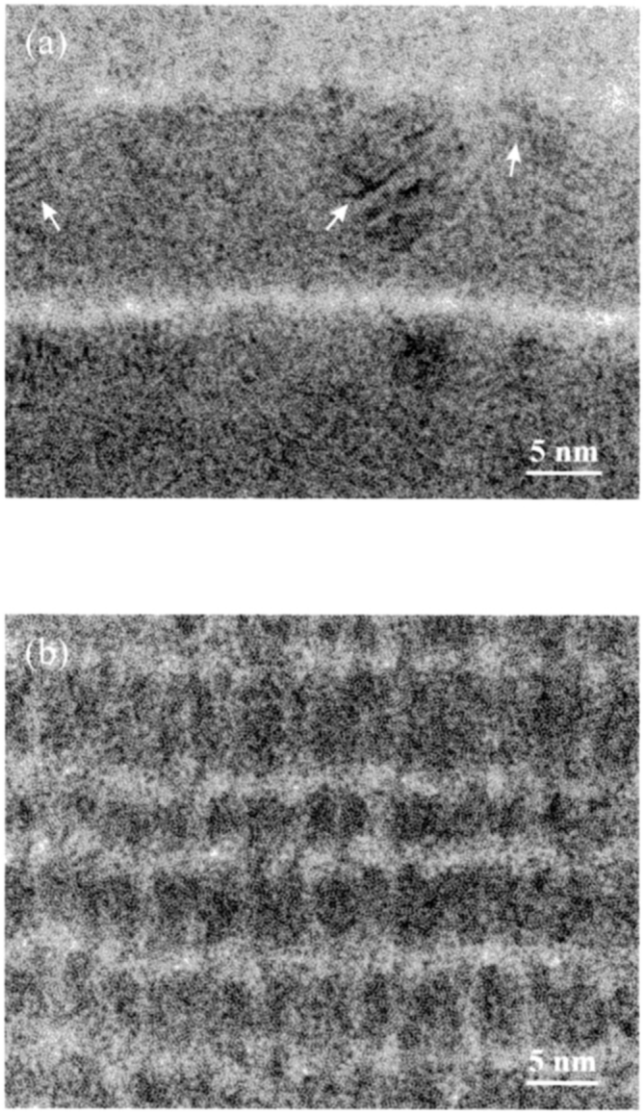

Fig. 8. Cross-sectional high-resolution transmission electron microscopy micrograph of the interlaminar structure: (a) coating system S2 featuring the nano-crystalline clusters embedded in the WC rich lamellae; (b) coating system T1 displaying the truly amorphous lamellae structure. On both micrographs the brighter lamellae corresponds to carbon rich. The arrows mark the position of some nano-crystalline clusters identified as having the cubic β-WC_{1-x} phase.

3.3. Defect structure

The coating systems exhibited two types of defects that are prone to jeopardise their mechanical properties. They were induced either by substrate surface irregularities or simply by the top morphology of the chromium columns. The defects produced by the substrate ridged surface were transferred through and magnified by the coating. Their growth structure was a direct consequence of the geometric shadowing because the high points on the growing surface received more coating flux than the valleys [20]. Moreover, the use of low ion bombardment with a small fraction of resputtering was not able to produce planar surfaces. Thus, macroboundaries (defects) developed at the lower chromium surface within a groove, and at either side of a ridge (cf. Fig. 2b,f). The degree of openness is associated to the magnitude of the surface irregularity from where it was originated. Fig. 9 and inset, displays a XTEM and HRTEM micrographs of two macroboundaries created by a substrate ridge. Although the macroboundaries in the micrograph are due to the existence of a ridge, they were enhanced by the convex shaped cusps formed by the two adjacent chromium columns at the rim of the ridge. These cusps were reproduced by each individual layer because the coating did not loose the memory of the earlier steps in its

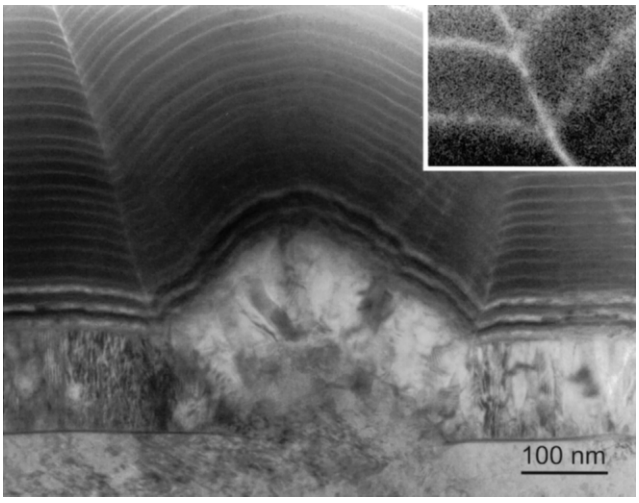

Fig. 9. Cross-sectional transmission electron microscopy micrograph of the macroboundaries created by a substrate surface ridge. The high-resolution inset shows the convex shaped cusps produced by two adjacent chromium columns at the rim of the ridge.

growth, as can be seen in the inset. Another type of defect, however, with a much smaller length scale, were formed whenever the chromium columns had a strongly faceted top morphology, resulting in deeper and sharper cusps between two adjacent columns. These planar defects propagated from the cusp minimum, but often only through the intermultilayer. They were ceased by the growth of the WC layer. Others had a longer path but never reaching the interface with the WC/C multilayer structure (cf. Fig. 6).

Chemical information on the defects was extracted from transmitted electron energy filtering micrographs recorded under high-resolution conditions. Fig. 10a,b shows a carbon image mapping recorded using the C–K edge and the corresponding compositional profile taken perpendicular to the defect. The width of integration perpendicular to the resulting profile is a trade-off between resolution and noise. However, a good compromise was obtained by a 100 pixel width (100 pixel equals 214.5 nm). The carbon compositional profile demonstrates that there is enrichment along the defect, which must be caused by carbon segregation during the deposition process. Therefore, it is concluded that the macroboundaries and planar defects are composed by the lower mass-thickness material present in the coating. The short path of the planar defects is related to the non-existence of free carbon in the WC layer to stabilise their propagation.

4. Conclusions

In this work the microstructure of WC/C coatings deposited on stainless steel and tool steel have been investigated. The main results are:

- The interfacial region between the crystalline steel substrate and the columnar chromium consists of an amorphous high-atomic-density phase.
- The coating structure is constituted by a body centred cubic chromium columnar interlayer, an amorphous intermultilayer of WC and carbon, an amorphous WC layer, and finally the amorphous interlaminar WC/C structure.
- One of the differences between the coatings is the thickness of a ribbon with a higher tungsten concentration after the intermultilayer. This layer is employed to improve the load capacity of the coating. However, it also has a direct influence on the elastic properties of the coatings, which are inversely proportional to the band thickness.
- Although the coatings are found to be primarily amorphous, crystalline particles are present, namely, nano-polycrystalline chromium carbides in the carbon layers of the intermultilayer; cubic β-WC_{1-x} in the WC interlayer, and clusters of cubic β-WC_{1-x} phase in the WC lamellae of the interlaminar WC/C.
- Defect structures were generated by the presence of substrate surface irregularities and by the top morphology of the chromium columns. Both types

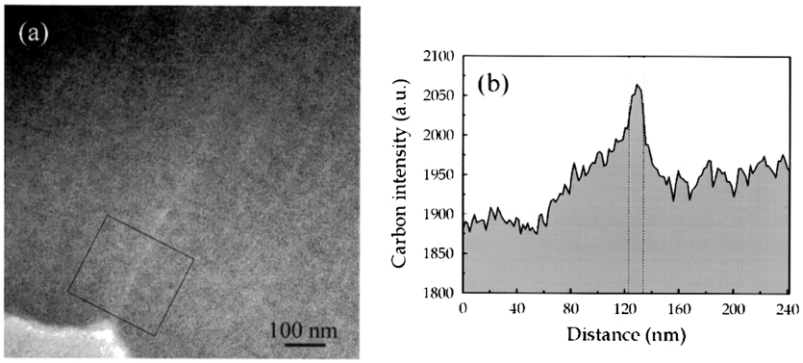

Fig. 10. (a) Cross-sectional transmission electron microscopy carbon mapping micrograph of a defect from coating system T1; (b) compositional carbon profile across the defect for an integration width of 100 pixels (214.3 nm). The dash lines delimit the defect width measured from the zero loss image.

of defects are mainly composed of carbon. It is evidence that the presence of a WC interlayer is beneficial for defect truncation because of the non-existence of free carbon to stabilise their propagation.

Acknowledgements

The work described in this paper has been founded by TNO Institute of Industrial Technology. The deposition of PVD WC/C coatings on steel substrates by Balzers Group is acknowledged.

References

[1] A. Erdemir, G.R. Fenske, R.A. Erck, Surf. Coat. Technol. 43/44 (1990) 588.
[2] J.-P. Hirvonen, J. Koskinen, J.R. Jervis, M. Nastasi, Surf. Coat. Technol. 80 (1996) 139.
[3] A. Raveh, L. Martinu, H.M. Hawthorne, M.R. Wertheimer, Surf. Coat. Technol. 58 (1993) 45.
[4] J. Franks, K. Enke, A. Richardt, Metals Mater. (1990) 695.
[5] Y. Liu, A. Erdemir, E.I. Meletis, Surf. Coat. Technol. 82 (1996) 48.
[6] E.G. Spencer, P.H. Schmidt, D.C. Joy, F.J. Sansalone, Appl. Phys. Lett. 129 (1976) 118.
[7] H. Tsai, D.B Bogy, J. Vac. Sci. Technol. A5 (1987) 3287.
[8] M. Ham, K.A. Lou, Vac. Sci. Technol. A8 (1990) 2143.
[9] O. Wänstrand, M. Larsson, P. Hedenqvist, Surf. Coat. Technol. 111 (1999) 247.
[10] J. Güttler, J. Reschke, Surf. Coat. Technol. 60 (1993) 531.
[11] A. Matthews, S.S. Eskildesn, Diam. Relat. Mater. 3 (1994) 902.
[12] G. Farges, J.P. Bosch, Wear 135 (1989) 1.
[13] M. Prutton, L.A. Larson, H. Poppa, J. Appl. Phys. 54 (1983) 374.
[14] B.D. Cullity, Elements of X-ray Diffraction, Addison-Wesley, Reading, MA, 1978.
[15] J.W. Edington, Interpretation of Transmission Electron Micrographs, MacMillan, London, 1975, p. 65.
[16] A.J. Thornton, J. Vac. Sci. Technol. A4 (1986) 3059.
[17] A. Matthews, S.S. Eskildsen, Diam. Relat. Mater. 3 (1994) 902.
[18] P. Ramanlal, L.M. Sander, Phys. Rev. Lett. 54 (1985) 1828.
[19] L.E. Toth, Transition Metal Carbides and Nitrides, Academic Press, New York, 1971, p. 85.
[20] J.W. Patten, Thin Solid Films 63 (1979) 121.